



Supplementary Materials for
**Resolving spatial and energetic distributions of trap states in
metal halide perovskite solar cells**

Zhenyi Ni*, Chunxiong Bao*, Ye Liu, Qi Jiang, Wu-Qiang Wu, Shangshang Chen,
Xuezheng Dai, Bo Chen, Barry Hartweg, Zhengshan Yu,
Zachary Holman, Jinsong Huang†

*These authors contributed equally to this work.

†Corresponding author. Email: jhuang@unc.edu

Published 20 March 2020, *Science* **367**, 1352 (2020)

DOI: 10.1126/science.aba0893

This PDF file includes:

Materials and Methods
Supplementary Text
Figs. S1 to S16
Tables S1 to S3
References

Materials and Methods

Materials

Unless stated otherwise, all the materials and solvent were purchased from Sigma-Aldrich. Lead iodide (PbI_2) with the purities of 99.999% and 98.5% for the synthesis of perovskite films and single crystals respectively were purchased from Alfa Aesar. MAI and MABr were purchased from GreatCell Solar.

Synthesis of perovskite single crystals

The precursor solution for the synthesis of MAPbI_3 single crystals were prepared by dissolving MAI and PbI_2 with the molar ratio of 1:1 in γ -butyrolactone (GBL) at a concentration of 1.5 M. The solution was heated at 65 °C with magnetic stirring until the solutes fully dissolved. The MAPbI_3 bulk single crystals were synthesized by inverse temperature crystallization. The MAPbI_3 solution was filtered using PTFE filter with 0.2- μm pore size and injected into a vial. The vial was then placed on a hot plate at the temperature of 75 °C. The temperature was gradually increased to boost the growth of the single crystal. The MAPbI_3 thin single crystals were grown by a hydrophobic interface-confined lateral crystal growth method.(25) A PTAA solution with the concentration of 2 mg/ml in toluene was first spin-coated onto an indium tin oxide (ITO) glass substrate at 4000 r.p.m for 30s. The as-prepared PTAA film was thermally annealed at 100 °C for 10 min. Then a drop of MAPbI_3 solution was inserted into two PTAA/ITO substrates, which were then placed on a hot plate at the temperature of 80 °C for 1 h. The temperature was subsequently increased to 85 and 90 °C to further promote the growth of the thin single crystals. Finally, the two substrates were separated to obtain MAPbI_3 thin single crystals on PTAA/ITO substrates. For the synthesis of double-layer MAPbI_3 thin single crystals, a drop of MAPbI_3 solution was added on a pre-synthesized MAPbI_3 thin single crystal on the PTAA/ITO substrate which was used as a seed crystal for further crystal growth. Then the single crystal and the solution were covered by another prepared PTAA/ITO substrate and placed on a hot plat at the temperature of 90 °C for the growth of the double-layer single crystals. The mechanical polishing of the perovskite single crystals was accomplished by using Zona. 37-948 3M polishing papers with the roughness of 15, 3, 2 and 1 micrometer. The oxysalt treatment of the MAPbI_3 thin single crystal was

carried out by spin-coating 4 mM $(\text{C}_8\text{-NH}_3)_2\text{SO}_4$ solution in toluene/isopropyl alcohol mixture on the single crystal at 6000 r.p.m for 30s. The MAPbBr₃ bulk single crystals were synthesized in the same procedure with that for the MAPbI₃ bulk single crystals. 1.2 M MAPbBr₃ precursor solution was prepared by dissolving MABr and PbBr₂ with the molar ratio of 1:1 in dimethylformamide (DMF) solvent and then added into a vial on the hot plate for the crystallization of the single crystals.

Device fabrication

The silicon (Si) solar cell was fabricated based on a *p*-type ($\sim 0.94 \Omega\cdot\text{cm}$ with the dopant concentration of $\sim 1.6 \times 10^{16} \text{ cm}^{-3}$) crystalline Si *p*-Si wafer. The as-cut wafer was chemically polished with a 30% potassium hydroxide, followed by a RCA-B cleaning and buffered oxide etching. The wafer then went through a phosphorus oxychloride (POCl_3) diffusion process at 830 °C for 100 minutes. After the removal of the phosphosilicate glass (PSG) with diluted hydrofluoric acid, the wafer was screen printed with aluminum paste on one side and then fired in a belt furnace with peak temperature of 800 °C. Finally, a silver electrode with the thickness of 120 nm was thermally evaporated on the other side to complete the device.

The perovskite bulk single crystal devices were fabricated by depositing Au electrodes (50 nm) on one side of the single crystals and C₆₀ (90 nm), BCP (6 nm) and Cu electrodes (80 nm) on the other side *via* thermal evaporation. The perovskite thin single crystal devices were fabricated by sequentially thermal evaporating C₆₀ (25 nm), BCP (6 nm) and Cu electrodes (80 nm) on perovskites that grown on the PTAA/ITO substrates. For the fabrication of ITO/PTAA/MAPbI₃/C₆₀/BCP/Cu polycrystalline thin film solar cells, ITO glass substrates were first prepared by cleaning with detergent, deionized water, acetone and isopropanol (IPA) in sequence and ultraviolet ozone treatment (20 min). A PTAA solution with the concentration of 2 mg/ml in toluene was spin-coated onto the ITO glass substrate at 4000 r.p.m for 30s. The as-prepared PTAA film was thermally annealed at 100 °C for 10 min. A 50 μl 1.3M MAPbI₃ precursor solution in DMF and dimethyl sulfoxide (DMSO) (with the volume ratio of 9:1) was spin-coated onto the PTAA at 2000 rpm for 2s and then 4000 rpm for 20s. During the spin-coating, 130 μl toluene was added into the film. The as-formed film was then heated at 65 °C for

10 min and 100 °C for 10 min. The whole device was completed by sequentially thermal evaporating C₆₀ (25 nm), BCP (6 nm) and Cu electrodes (80 nm) on the perovskite film. The ITO/PTAA/Cs_{0.05}FA_{0.70}MA_{0.25}PbI₃/C₆₀/BCP/Cu perovskite solar cells were fabricated with the methods used in ref (30). The FA_{0.92}MA_{0.08}PbI₃ polycrystalline thin films are fabricated by using the methods reported in ref (34). The Rb_{0.05}Cs_{0.05}FA_{0.75}MA_{0.15}Pb(I_{0.95}Br_{0.05})₃ and Cs_{0.05}FA_{0.8}MA_{0.15}Pb_{0.5}Sn_{0.5}(I_{0.85}Br_{0.15})₃ thin films are fabricated by using similar methods used in refs (36) and (37), respectively.

Device characterization

The standard C - V , DLCP and TAS measurements were performed by using an Agilent E4980A precision LCR meter. For the standard C - V measurement, the DC bias was scanning from 0 V to the V_{OC} (e.g., 1.1 V) for the perovskite solar cells. The amplitude of the AC bias was 20 mV. The DLCP measurement were conducted in the same DC bias range with that for the standard C - V measurement. While the amplitude of the AC biases were ranging from 20 to 200 mV. For each AC bias, an additional offset DC voltage was applied to keep the maximum forward bias constant. The measured capacitances at each DC bias were gathered with a homemade computer program and fitted with a polynomial function to obtain C_0 and C_1 . For the comparison of the trap densities, the trap densities measured at 10 kHz are representatively given, which would not affect the comparison of the relative values as the trap densities are basically on the same order of magnitude with the change of the AC frequency in the vicinity of 10 kHz. For the TAS measurement, the DC bias was fixed at 0 V and the amplitude of the AC bias was 20 mV. The scanning range of the AC frequency was 0.02 – 2000 kHz. The tDOS ($N_T(E_\omega)$) is calculated by using equation $N_T(E_\omega) = -\frac{1}{qkT} \frac{\omega dC}{d\omega} \frac{V_{bi}}{W}$, where W and V_{bi} are the depletion width and build-in potential, respectively, which were derived from the Mott-Schottky analysis of the C - V measurement. q , k , T , ω and C are elementary charge, Boltzmann's constant, temperature, angular frequency and specific capacitance, respectively. The demarcation energy $E_\omega = kT \ln\left(\frac{\omega_0}{\omega}\right)$ (where ω_0 is the attempt-to-escape angular frequency that equals to $2\pi\nu_0 T^2$ (ν_0 is the temperature-independent attempt-to-escape frequency)) is derived from the temperature-dependent C - f

measurements which were carried out in a Lake Shore Cryotronics probe stage with a Lake Shore Cryotronics temperature controller model 336. SMA connected cables and ZN50R DC/RF probes that were applicable for RF test up to 1 GHz were equipped with the probe station. Before each measurement, the system was self-calibrated under open-circuit and short-circuit conditions to compensate any undesired signal from the instrument. The capacitance of the instrument and cables is in the range of 10 – 300 aF when the AC frequency changes from 0.02 to 2000 kHz. The ν_0 is obtained from the fitting of $\ln\left(\frac{T^2}{\omega}\right) = \frac{E_T}{kT} - \ln(2\pi\nu_0)$ obtained at different T . The ω_0 of the MAPbI₃ thin single crystal and the Cs_{0.05}FA_{0.70}MA_{0.25}PbI₃ thin film are 1.9×10^{10} Hz and 1.0×10^{12} Hz, respectively. All the measurements were finished in dark conditions.

The J - V curves of the solar cells were recorded with a Keithley 2400 Source Meter under simulated AM 1.5G irradiation that produced by a Xenon-lamp-solar simulator (Oriel Sil3A Class AAA Solar Simulator). The light intensity was calibrated by a referential Si solar cell equipped with a SCHOTT visible color KG5 glass filter (Newport 91150V). SEM measurements were performed by using the FEI Helios 600 Nanolab Dual Beam System at an acceleration voltage of 5 kV. TEM measurements were performed by using the FEI Talos F200X at an acceleration voltage of 200 kV. To avoid possible damage of the perovskite by the electron beam, a low electron dose of $7.8 \text{ e } \text{\AA}^2$ was applied during the measurement. A Bruker Dektak XT stylus profiler was used to measure the thickness of the perovskite single crystals and thin films.

SCAPS simulation

A basic planar structure of HTL/perovskite/ETL was constructed for the solar cell simulations.⁽³⁸⁾ The solar cells were simulated with a AM 1.5G solar spectrum that was implanted in the software. Three trap centers I, II and III with the trap depths close to the measured values by DLPC and TAS were introduced to the perovskite layer during the simulations. Trap I and II with shallower depths were assumed to be uniformly distributed in the whole film, while trap III with a deeper depth was distributed both inside and at the interface of the perovskite film, of which the distribution was described by a Beta-function implanted in the software. As a result, the bulk traps contains trap I, II

and the bulk component of trap III, while the interface trap refers to the interface component of trap III only.

Supplementary Text

Drive-level capacitance profiling technique

The derivation of the carrier density including deep trap states is based on the nonlinear relationship between the change of charges (δQ) and the perturbation AC bias (δV): (23)

$$\delta Q/\delta V = C_0 + C_1\delta V + C_2(\delta V)^2 + \dots \quad (1)$$

The DLCP method uses a series of variable δV (e.g., 20 to 200 mV) to measure the junction capacitance and acquire the capacitance contribution from the trap states by taking advantage of the information embedded in the higher order terms. With the determination of C_0 and C_1 , the carrier density (N) that includes both free carrier density (N_0) and trap density (N_T) at a certain position X from the junction barrier is calculated by:

$$N = -\frac{C_0^3}{2q\epsilon A^2 C_1}, \quad (2)$$

where q is the elementary charge, ϵ is the dielectric constant of the semiconductor and A is the active area of the junction. The position X is defined to be the location at which a trap state with the depth E_T equals to the demarcation energy E_ω at a given AC frequency and temperature (T) that crosses the Fermi level (E_F) of the semiconductor. The emission rate (R) of a charge emitting from a trap state with the depth of E_T to the band edge is determined by: (39)

$$R = N_V(T)\langle v \rangle \sigma_h \exp\left(-\frac{E_T}{kT}\right), \quad (3)$$

where k is the Boltzmann's constant, $N_V(T)$ is the effective density of states of the valence band, $\langle v \rangle$ is the average thermal velocity and σ_h is the capture cross section of the trap state. Since only free carriers and trap states with R larger than the angular frequency (ω) of the δV will contribute to the junction capacitance, the critical depth of a trap state that is detectable by capacitance measurement is given by E_ω :

$$E_\omega = kT \ln\left(\frac{\omega_0}{\omega}\right), \quad (4)$$

where ω_0 is the attempt-to-escape angular frequency of the trap state, which equals to $2\pi\nu_0T^2$ (where $\nu_0T^2 = N_v(T) \langle v \rangle \sigma_h$). Any traps with the trap depth shallower than the critical value that is able to respond to the AC frequency is taken into account for the calculation of the total carrier density. The lower the applied AC frequency, the deeper the trap states that could be detected. A very high AC frequency could only detect rather shallow trap states and the free carriers. In this work, the free carrier density is estimated by measuring the carrier density at a high AC frequency when the total carrier density tend to saturate with the further increase of the AC frequency (e.g., 500 kHz). The trap density at a much lower AC frequency (large E_ω) can be estimated by subtracting the estimated free carrier density from the total carrier density measured at the low AC frequency. This allows us to derive the energetic distribution of trap states by tuning the frequency of δV or the T during the measurement. As the position X varies with the band bending of the semiconductor in the depletion region, we can readily tune X by applying a changing DC bias to the junction. Therefore, both the spatial and energetic distributions of trap states can be profiled by DLCP. The profiling distance from the junction barrier is given by $\varepsilon A/C_0$.(23)

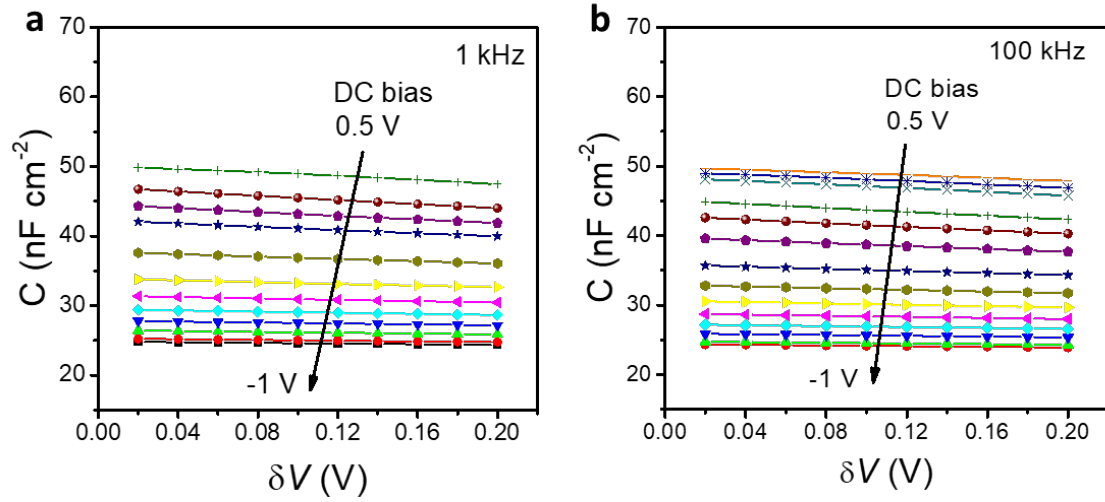


Fig. S1. Variation of the junction capacitance with the amplitude of the AC biases for a Si solar cell. Variation of the junction capacitance (C) of a Si solar cell with respect to the amplitude of the AC biases (δV) under different DC biases measured at AC frequencies of (a) 1 kHz and (b) 100 kHz .

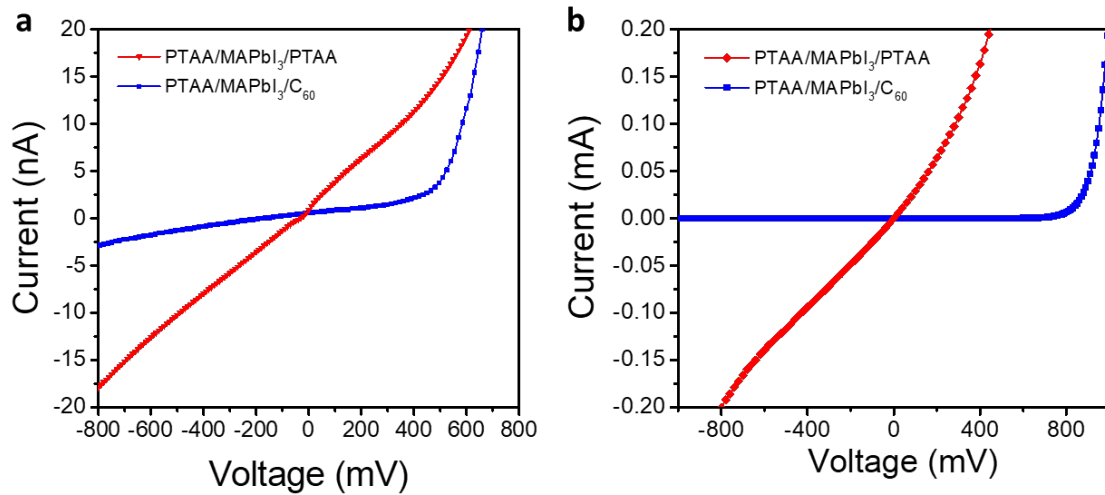


Fig. S2. I-V curves of (a) MAPbI₃ thin single crystal and (b) MAPbI₃ polycrystalline thin film devices with the device structures of ITO/PTAA (15 nm)/MAPbI₃/C₆₀ (25 nm)/BCP/Cu (blue curve) and ITO/PTAA (15 nm)/MAPbI₃/PTAA (15 nm)/Cu (red curve).

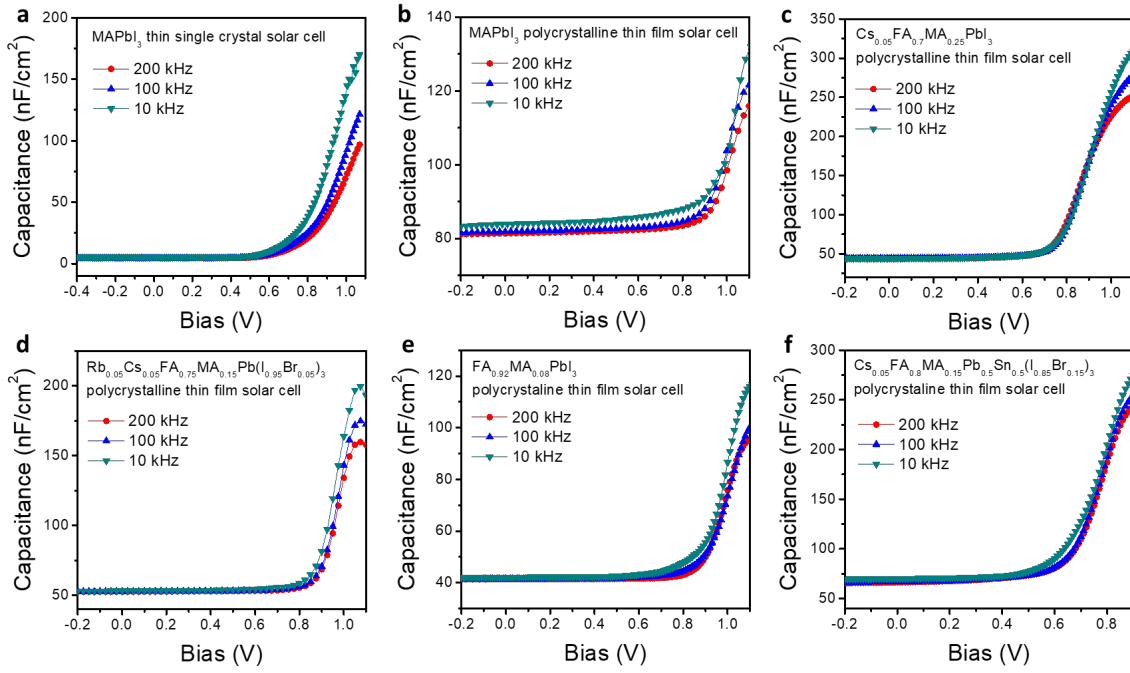


Fig. S3. C-V curves of planar structured perovskite solar cells. C-V curves of perovskite solar cells with the device structure of ITO/PTAA/perovskite/C₆₀/BCP/Cu measured in the work. (a) MAPbI₃ thin single crystal, (b) MAPbI₃ polycrystalline thin film, (c) Cs_{0.05}FA_{0.7}MA_{0.25}PbI₃ polycrystalline thin film, (d) Rb_{0.05}Cs_{0.05}FA_{0.75}MA_{0.15}Pb(I_{0.95}Br_{0.05})₃ polycrystalline thin film, (e) FA_{0.92}MA_{0.08}PbI₃ polycrystalline thin film and (f) Cs_{0.05}FA_{0.8}MA_{0.15}Pb_{0.5}Sn_{0.5}(I_{0.85}Br_{0.15})₃ polycrystalline thin film solar cells.

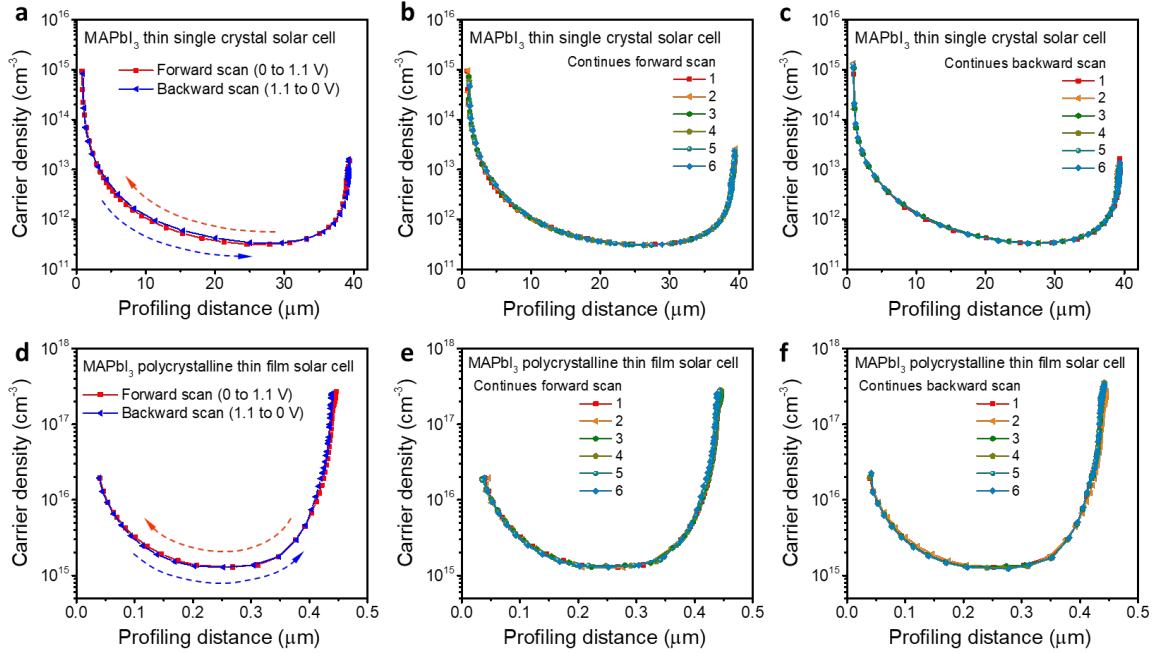


Fig. S4. Continues forward and backward DLCP scans. (a) Forward and backward scans of the DC bias for the DLCP measurement of a MAPbI₃ thin single crystal solar cell. (b) Continues forward and (c) continues backward scans of the DC bias for the DLCP measurement of the MAPbI₃ thin single crystal solar cell. (d) Forward and backward scans of the DC bias for the DLCP measurement of a MAPbI₃ polycrystalline thin film solar cell. (e) Continues forward and (f) continues backward scans of the DC bias for the DLCP measurement of the MAPbI₃ polycrystalline thin film solar cell. The AC frequency is 10 kHz.

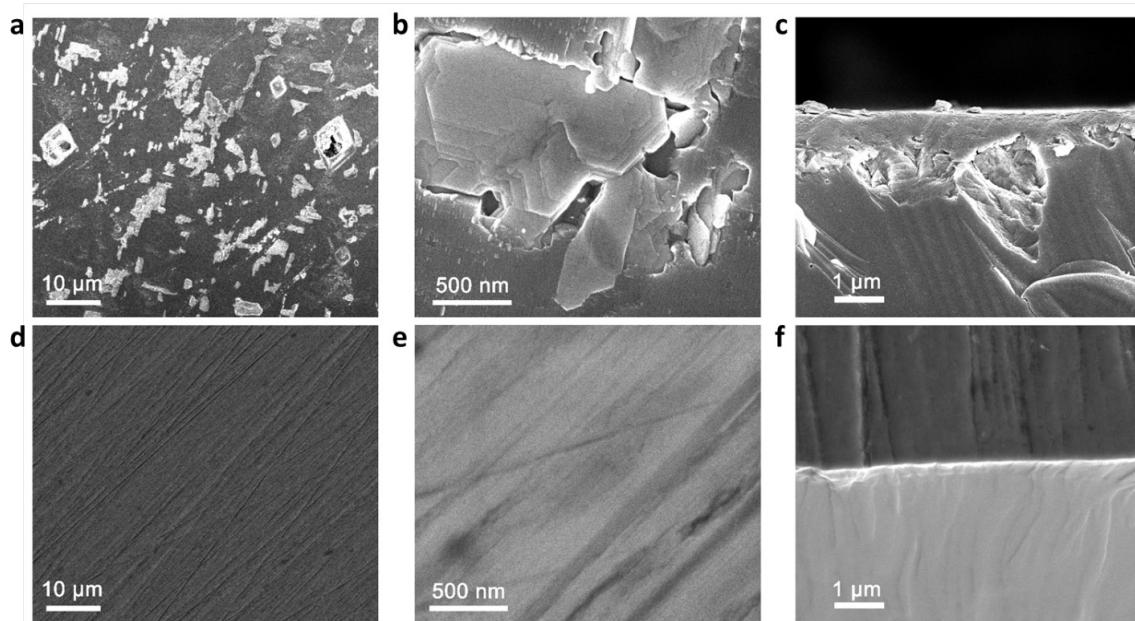


Fig. S5. SEM images of a MAPbI₃ bulk single crystal before and after mechanical polishing. (a), (b) top-view and (c) cross-sectional SEM images of a bulk MAPbI₃ single crystal before mechanical polishing. (d), (e) top-view and (f) cross-sectional SEM images of the bulk MAPbI₃ single crystal after mechanical polishing.

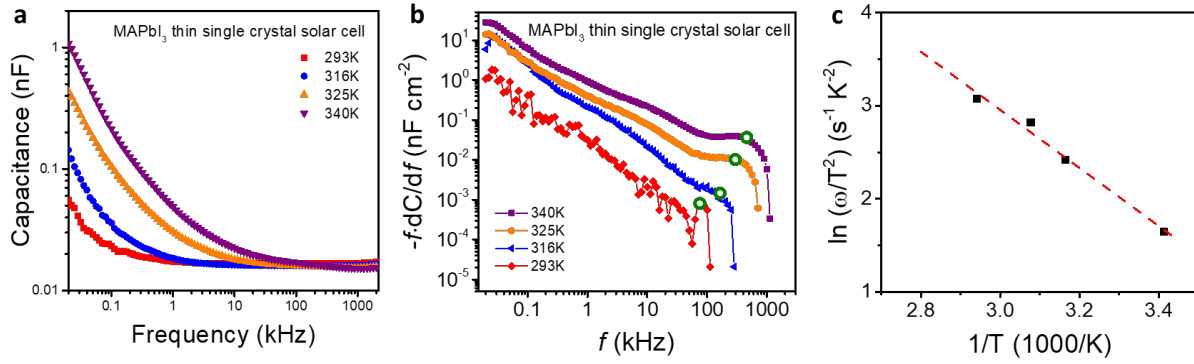


Fig. S6.

TAS measurement for a MAPbI₃ thin single crystal device. (a) C - f curves of a MAPbI₃ thin single crystal solar cells measured at different temperatures. (b) The derivative specific capacitance (C) with respect to the frequency (f) of the MAPbI₃ thin single crystal device at different temperatures. The DC and AC biases are 0 V and 0.02 V, respectively. The peak positions of the trap states are denoted by green circles for clarity. (c) Arrhenius plot of the characteristic frequencies at different temperatures extracted from the derivative specific capacitance spectra.

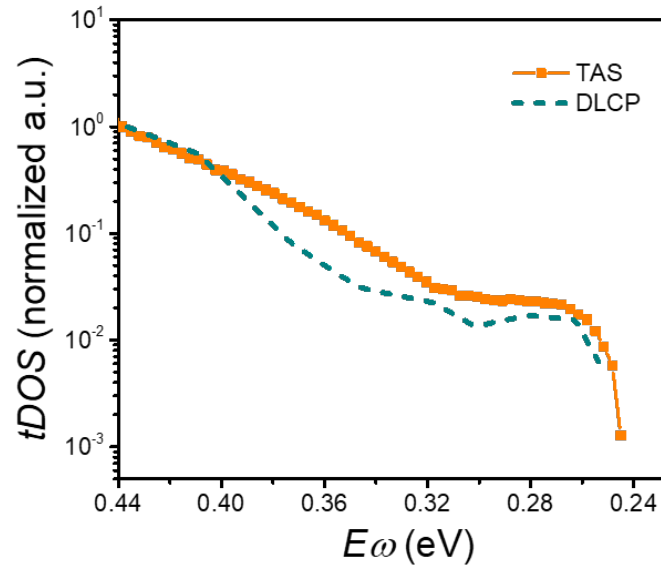


Fig. S7.

tDOS measured by TAS and derived from DLCP results at the DC bias of 0 V for a MAPbI₃ thin single crystal solar cell.

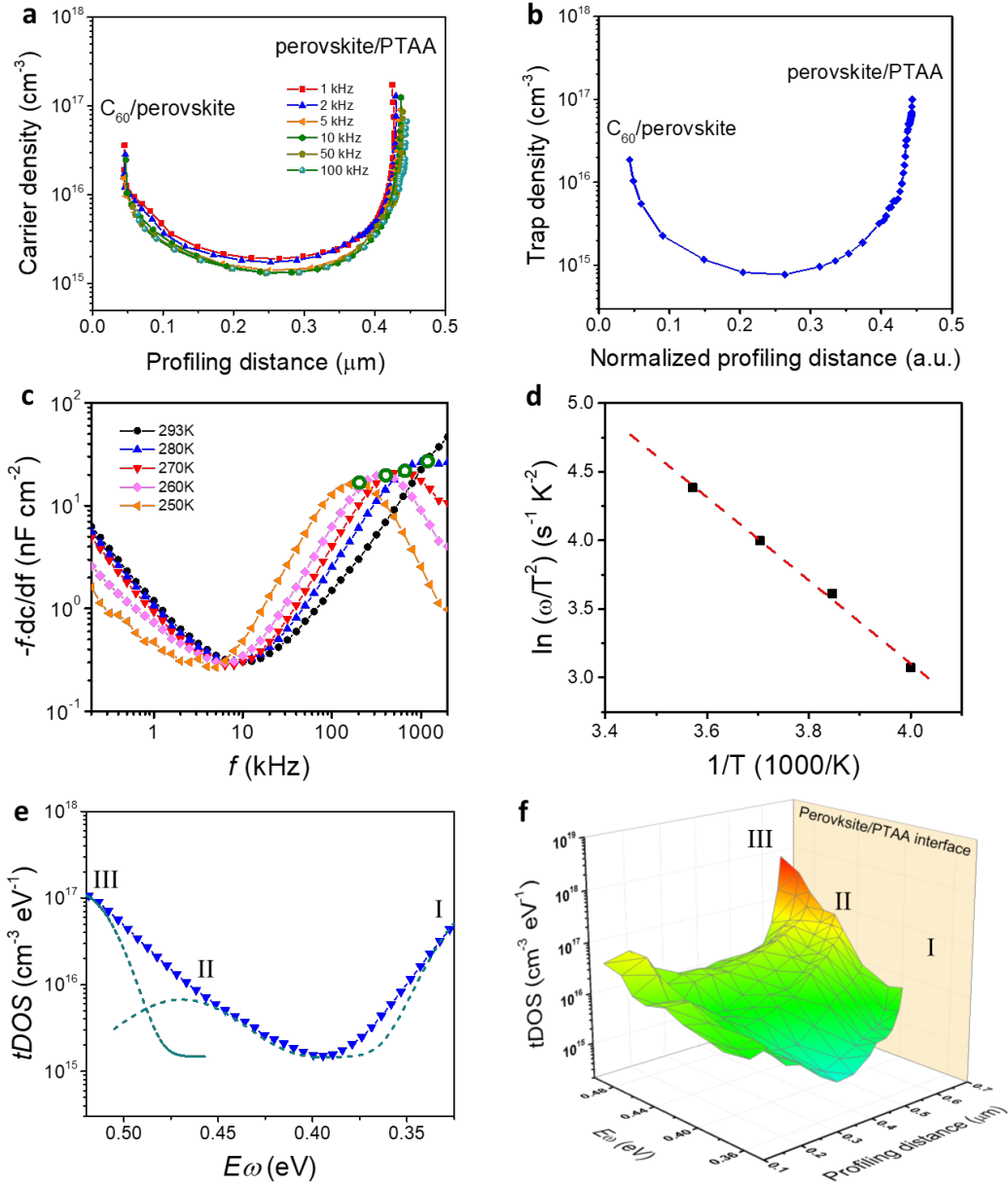


Fig. S8.

DLCP and TAS measurement results of a MAPbI₃ polycrystalline thin film solar cell. (a) Dependence of the carrier density on the profiling distance for a MAPbI₃ polycrystalline thin film solar cell measured at different AC frequencies by DLCP. (b) Dependence of the trap density on the profiling distance for the MAPbI₃ thin film in the solar cell at the AC frequency of 10 kHz measured by DLCP. (c) The derivative specific capacitance (C) with respect to the frequency (f) of the MAPbI₃ thin film device at different temperatures. The DC and AC biases are 0 V and 0.02 V, respectively. (d) Arrhenius plot of the characteristic frequencies at different temperatures extracted from the derivative specific capacitance spectra. (e) tDOS of the MAPbI₃ thin film solar cell measured by TAS method. (f) Spatial and energy mapping of the density of trap states of the MAPbI₃ thin film in the solar cell measured by DLCP.

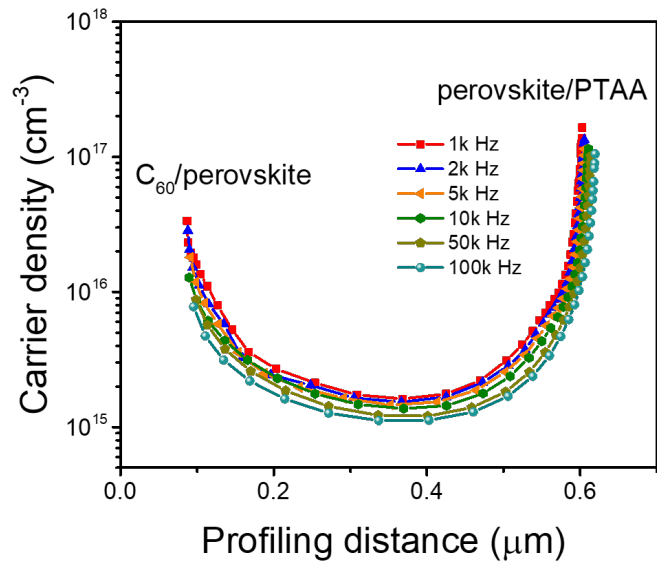


Fig. S9.

Spatial distribution of carrier densities in the perovskite thin film. Dependence of the carrier density on the profiling distance for the $\text{Cs}_{0.05}\text{FA}_{0.70}\text{MA}_{0.25}\text{PbI}_3$ thin film in the device of ITO/PTAA/ $\text{Cs}_{0.05}\text{FA}_{0.70}\text{MA}_{0.25}\text{PbI}_3$ / C_{60} /BCP/Cu measured at different AC frequencies by DLCP.

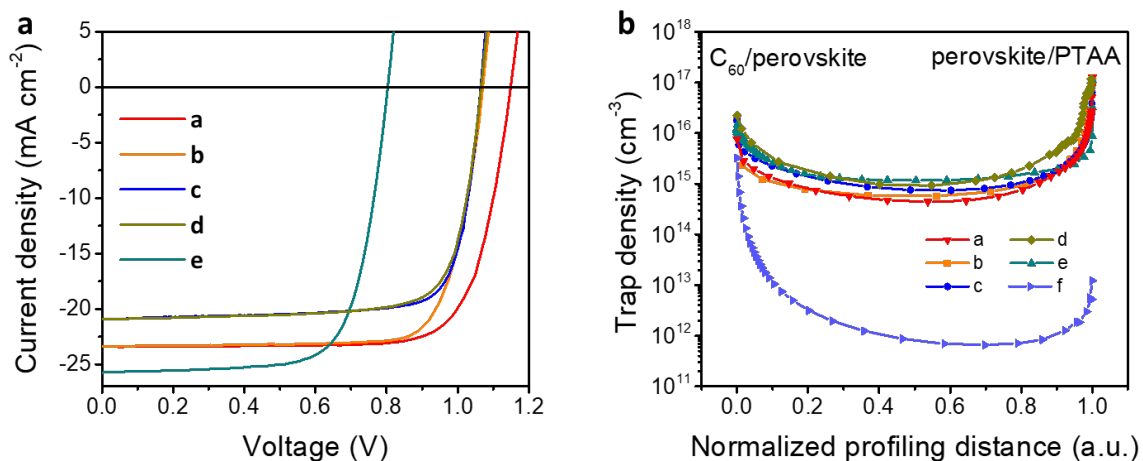


Fig. S10.

Trap density distributions in perovskite polycrystalline thin films and thin single crystal with different compositions. (a) Current density – voltage ($J - V$) curves of polycrystalline perovskite thin film solar cells with different perovskite compositions. (b) Dependence of the trap density on the profiling distance for polycrystalline perovskite thin films with different compositions and a 20 μm thick MAPbI_3 single crystal. The trap densities are measured at the AC frequency of 10 kHz. The compositions of the polycrystalline thin films and the single crystal: a. $\text{Cs}_{0.05}\text{FA}_{0.70}\text{MA}_{0.25}\text{PbI}_3$, b. $\text{Rb}_{0.05}\text{Cs}_{0.05}\text{FA}_{0.75}\text{MA}_{0.15}\text{Pb}(\text{I}_{0.95}\text{Br}_{0.05})_3$, c. $\text{FA}_{0.92}\text{MA}_{0.08}\text{PbI}_3$, d. MAPbI_3 , e. $\text{Cs}_{0.05}\text{FA}_{0.8}\text{MA}_{0.15}\text{Pb}_{0.5}\text{Sn}_{0.5}(\text{I}_{0.85}\text{Br}_{0.15})_3$ and f. MAPbI_3 thin single crystal.

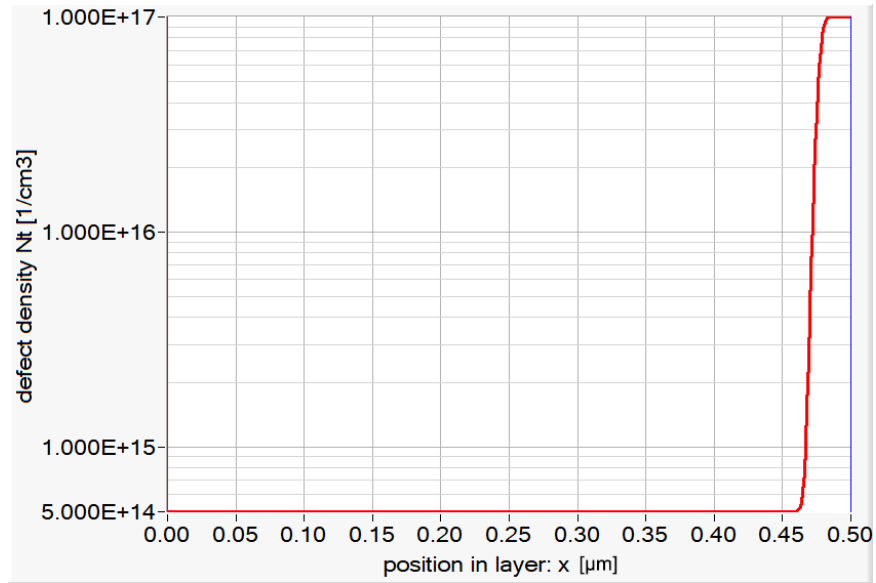


Fig. S11.

Spatial distribution of trap III in a MAPbI₃ thin film used for the SCAPS simulations. Bulk trap density of $5.0 \times 10^{14} \text{ cm}^{-3}$ and interface trap density of $1.0 \times 10^{17} \text{ cm}^{-3}$ are representatively shown.

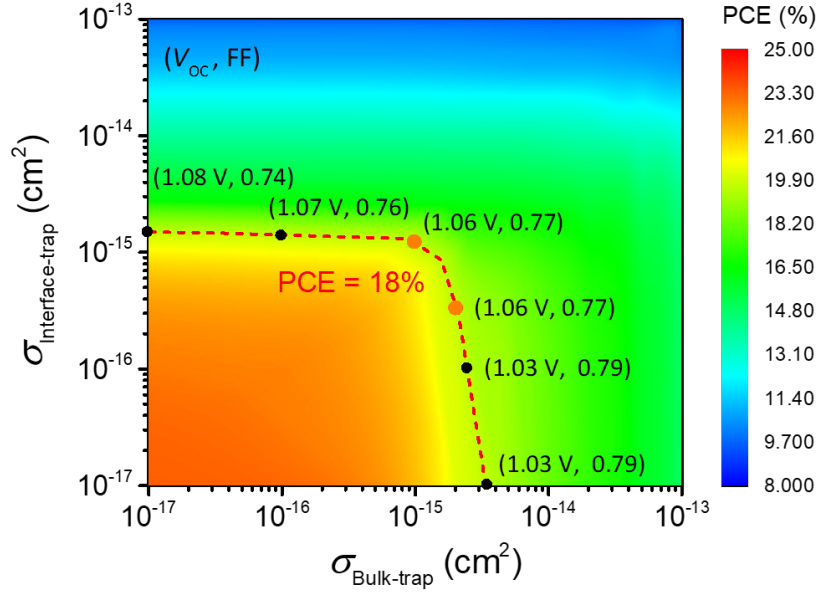


Fig. S12.

Dependence of the PCE of a MAPbI₃ polycrystalline thin film solar on capture cross sections of traps. Dependence of the simulated PCE of a MAPbI₃ polycrystalline thin film solar cell on the capture cross sections of the interface traps ($\sigma_{\text{Interface-trap}}$) and bulk traps ($\sigma_{\text{Bulk trap}}$). The DLCP measured interface and bulk trap densities were adopted for the simulation. The red dashed line denotes the contour line corresponding to the PCE of 18%. The numbers in the brackets show the V_{OC} and FF (V_{OC} , FF) of the devices with the $\sigma_{\text{Interface-trap}}$ and $\sigma_{\text{Bulk trap}}$ marked by the dots. Only when the $\sigma_{\text{Interface-trap}}$ is in the range of $\sim 3 \times 10^{-16} \text{ cm}^2$ to $1 \times 10^{-15} \text{ cm}^2$ and the $\sigma_{\text{Bulk trap}}$ is in the range of $\sim 1 \times 10^{-15} \text{ cm}^2$ to $2 \times 10^{-15} \text{ cm}^2$, the simulated V_{OC} and FF fit well with the experimental results.

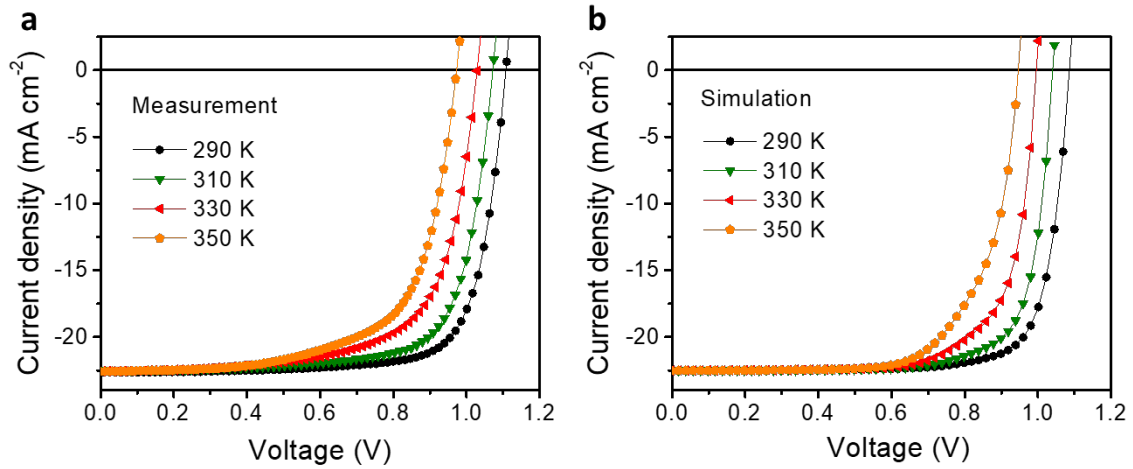


Fig. S13.

Temperature-dependent J - V curves of a MAPbI₃ polycrystalline thin film solar cell.

(a) Measured J - V curves of a MAPbI₃ polycrystalline thin film solar cell at different temperatures. (b) Simulated J - V curves of a MAPbI₃ polycrystalline thin film solar cell with the trap density and distribution extrapolated from the DLCP results at different temperatures.

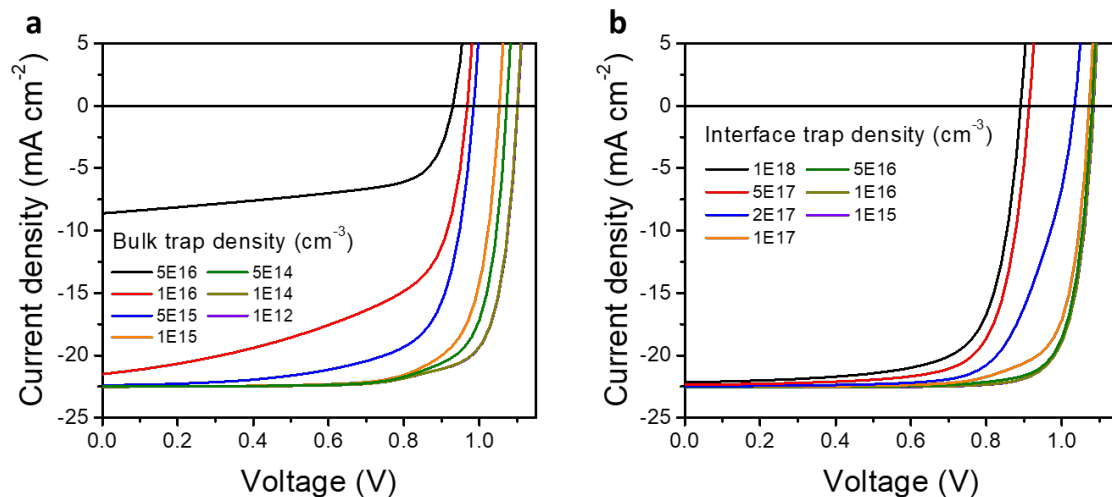
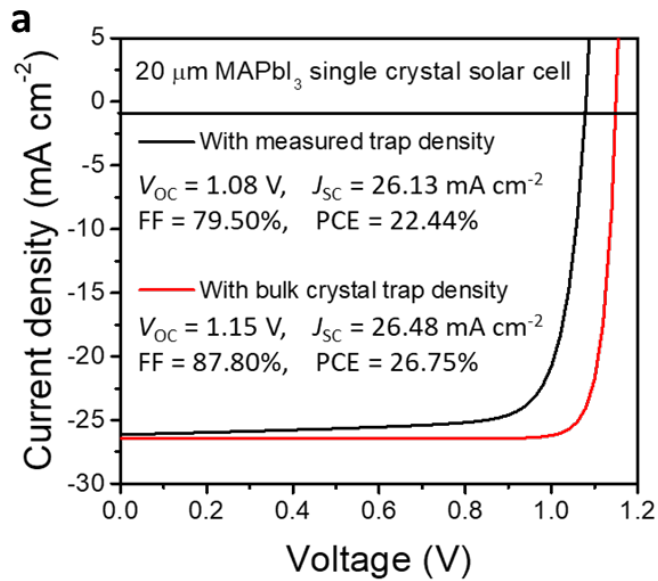


Fig. S14.

Simulated influence of the trap density on the performance of MAPbI₃ thin film solar cells. (a) Simulated influence of the bulk trap density on the performance of the MAPbI₃ thin film solar cell. The bulk trap density varies from $1.0 \times 10^{12} \text{ cm}^{-3}$ to $5.0 \times 10^{16} \text{ cm}^{-3}$ and the interface trap density is kept at $1.0 \times 10^{17} \text{ cm}^{-3}$. (b) Simulated influence of the interface trap density on the performance of the MAPbI₃ thin film solar cell. The interface trap density varies from $1.0 \times 10^{15} \text{ cm}^{-3}$ to $1.0 \times 10^{18} \text{ cm}^{-3}$ and the bulk trap density is kept at $5.0 \times 10^{14} \text{ cm}^{-3}$.



b

	Trap I	Trap II	Trap III
Capture cross section electrons (cm^2)	1.00E-15	1.00E-15	1.00E-15
Capture cross section holes (cm^2)	1.00E-15	1.00E-15	1.00E-15
Energetic distribution	Gaussian	Gaussian	Gaussian
Depth with respect to VB	0.10	0.18	0.40
Position dependence	Uniform	Uniform	Beta-function
Trap density in thin single crystal ($1/\text{cm}^3$)	8E11	8E11	8E11 + 2E15
Trap density in bulk single crystal ($1/\text{cm}^3$)	2E11	2E11	2E11 + 2E12

Fig. S15.

Simulated $J - V$ curves for MAPbI₃ thin single crystal solar cells. (a) Simulated $J - V$ curves of a 20- μm -thick MAPbI₃ single crystal solar cell with the measured trap densities from the thin single crystal and the bulk crystal, respectively. (b) The parameters of the trap states in the MAPbI₃ single crystal used for the solar cell simulations with the SCAPS.

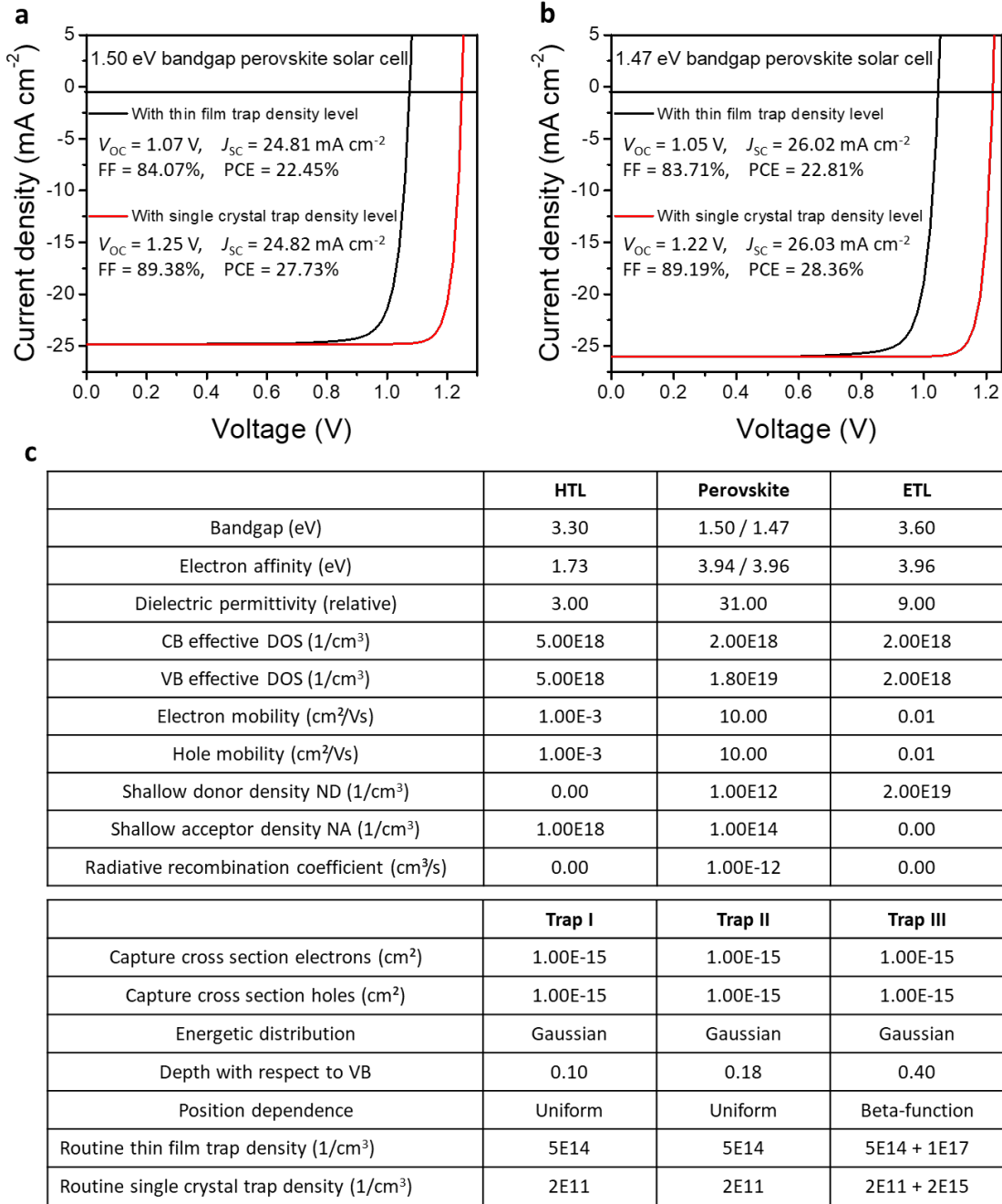


Fig. S16.

SCAPS simulations for low bandgap perovskite solar cells. (a) Simulated $J-V$ curves of a 1.50 eV-bandgap perovskite solar cell varied trap densities. (b) Simulated $J-V$ curves of a 1.47 eV-bandgap perovskite solar cell varied trap densities. (c) The parameters used for the solar cell simulations with the SCAPS.

Table S1.

The open circuit voltage (V_{OC}), short circuit current density (J_{SC}), fill factors (FF) and power conversion efficiency (PCE) of polycrystalline perovskite thin film solar cells with different compositions.

Composition	V_{OC} (V)	J_{SC} (mA cm ⁻²)	FF (%)	PCE (%)
a. Cs _{0.05} FA _{0.70} MA _{0.25} PbI ₃ film	1.15	23.39	77.39	20.82
b. Rb _{0.05} Cs _{0.05} FA _{0.75} MA _{0.15} Pb(I _{0.95} Br _{0.05}) ₃ film	1.06	23.40	79.51	19.72
c. FA _{0.92} MA _{0.08} PbI ₃ film	1.06	21.51	78.41	17.88
d. MAPbI ₃	1.05	21.78	77.42	17.79
e. Cs _{0.05} FA _{0.8} MA _{0.15} Pb _{0.5} Sn _{0.5} (I _{0.85} Br _{0.15}) ₃ film	0.81	25.76	72.15	15.05

Table S2.

Basic parameters of the PTAA, MAPbI₃ and C₆₀ layers for the simulations of p-i-n structure solar cells with the SCAPS package.

	PTAA	MAPbI₃	C₆₀
Thickness (nm)	10	500	25
Bandgap (eV)	3.30	1.55	1.90
Electron affinity (eV)	1.80	3.93	4.10
Dielectric permittivity (relative)	3.00	31.00	5.00
CB effective DOS (1/cm ³)	5.00E18	2.00E18	2.00E18
VB effective DOS (1/cm ³)	5.00E18	1.80E19	2.00E18
Electron thermal velocity (cm/s)	1.00E7	1.00E7	1.00E7
Hole thermal velocity (cm/s)	1.00E7	1.00E7	1.00E7
Electron mobility (cm ² /Vs)	1.00E-3	10.00	0.01
Hole mobility (cm ² /Vs)	1.00E-3	10.00	0.01
Shallow donor density ND (1/cm ³)	0.00	1.00E12	2.00E18
Shallow acceptor density NA (1/cm ³)	2.00E17	1.00E14	0.00
Radiative recombination coefficient (cm ³ /s)	0.00	1.00E-12	0.00

Table S3.

Parameters of trap states in the MAPbI₃ for the simulations of p-i-n structure solar cells with the SCAPS package.

	Trap I	Trap II	Trap III
Defect type	Single acceptor	Single acceptor	Single acceptor
Capture cross section electrons (cm ²)	1.00E-15	1.00E-15	1.00E-15
Capture cross section holes (cm ²)	1.00E-15	1.00E-15	1.00E-15
Energetic distribution	Gaussian	Gaussian	Gaussian
Depth with respect to valence band	0.25	0.36	0.60
Position dependence	Uniform	Uniform	Beta-function
Total density (1/cm ³)	Variable	Variable	Variable
Routine trap density in thin film (1/cm ³)	5E14	5E14	5E14 + 1E17
Routine trap density in single crystal (1/cm ³)	2E11	2E11	2E11 + 2E15

References and Notes

1. N.-G. Park, Perovskite solar cells: An emerging photovoltaic technology. *Mater. Today* **18**, 65–72 (2015). [doi:10.1016/j.mattod.2014.07.007](https://doi.org/10.1016/j.mattod.2014.07.007)
2. L. M. Herz, Charge-carrier mobilities in metal halide perovskites: Fundamental mechanisms and limits. *ACS Energy Lett.* **2**, 1539–1548 (2017). [doi:10.1021/acseenergylett.7b00276](https://doi.org/10.1021/acseenergylett.7b00276)
3. Q. Dong, Y. Fang, Y. Shao, P. Mulligan, J. Qiu, L. Cao, J. Huang, Electron-hole diffusion lengths >175 μm in solution-grown $\text{CH}_3\text{NH}_3\text{PbI}_3$ single crystals. *Science* **347**, 967–970 (2015). [doi:10.1126/science.aaa5760](https://doi.org/10.1126/science.aaa5760) [Medline](#)
4. C. Gehrman, D. A. Egger, Dynamic shortening of disorder potentials in anharmonic halide perovskites. *Nat. Commun.* **10**, 3141 (2019). [doi:10.1038/s41467-019-11087-y](https://doi.org/10.1038/s41467-019-11087-y) [Medline](#)
5. S. B. Zhang, S.-H. Wei, A. Zunger, Stabilization of ternary compounds via ordered arrays of defect pairs. *Phys. Rev. Lett.* **78**, 4059–4062 (1997). [doi:10.1103/PhysRevLett.78.4059](https://doi.org/10.1103/PhysRevLett.78.4059)
6. K. X. Steirer, P. Schulz, G. Teeter, V. Stevanovic, M. Yang, K. Zhu, J. J. Berry, Defect tolerance in methylammonium lead triiodide perovskite. *ACS Energy Lett.* **1**, 360–366 (2016). [doi:10.1021/acseenergylett.6b00196](https://doi.org/10.1021/acseenergylett.6b00196)
7. W.-J. Yin, T. Shi, Y. Yan, Unusual defect physics in $\text{CH}_3\text{NH}_3\text{PbI}_3$ perovskite solar cell absorber. *Appl. Phys. Lett.* **104**, 063903 (2014). [doi:10.1063/1.4864778](https://doi.org/10.1063/1.4864778)
8. C. Eames, J. M. Frost, P. R. Barnes, B. C. O'Regan, A. Walsh, M. S. Islam, Ionic transport in hybrid lead iodide perovskite solar cells. *Nat. Commun.* **6**, 7497 (2015). [doi:10.1038/ncomms8497](https://doi.org/10.1038/ncomms8497) [Medline](#)
9. A. Walsh, D. O. Scanlon, S. Chen, X. G. Gong, S. H. Wei, Self-regulation mechanism for charged point defects in hybrid halide perovskites. *Angew. Chem. Int. Ed.* **54**, 1791–1794 (2015). [doi:10.1002/anie.201409740](https://doi.org/10.1002/anie.201409740) [Medline](#)
10. G. J. Wetzelaer, M. Scheepers, A. M. Sempere, C. Momblona, J. Ávila, H. J. Bolink, Trap-assisted non-radiative recombination in organic-inorganic perovskite solar cells. *Adv. Mater.* **27**, 1837–1841 (2015). [doi:10.1002/adma.201405372](https://doi.org/10.1002/adma.201405372) [Medline](#)
11. W. Tress, N. Marinova, O. Inganäs, M. K. Nazeeruddin, S. M. Zakeeruddin, M. Graetzel, Predicting the open-circuit voltage of $\text{CH}_3\text{NH}_3\text{PbI}_3$ perovskite solar cells using electroluminescence and photovoltaic quantum efficiency spectra: The role of radiative and non-radiative recombination. *Adv. Energy Mater.* **5**, 1400812 (2015). [doi:10.1002/aenm.201400812](https://doi.org/10.1002/aenm.201400812)
12. J. M. Ball, A. Petrozza, Defects in perovskite-halides and their effects in solar cells. *Nat. Energy* **1**, 16149 (2016). [doi:10.1038/nenergy.2016.149](https://doi.org/10.1038/nenergy.2016.149)
13. T. Leijtens, E. T. Hoke, G. Grancini, D. J. Slotcavage, G. E. Eperon, J. M. Ball, M. De Bastiani, A. R. Bowring, N. Martino, K. Wojciechowski, M. D. McGehee, H. J. Snaith, A. Petrozza, Mapping electric field-induced switchable poling and structural degradation in hybrid lead halide perovskite thin films. *Adv. Energy Mater.* **5**, 1500962 (2015). [doi:10.1002/aenm.201500962](https://doi.org/10.1002/aenm.201500962)

14. C. Ran, J. Xu, W. Gao, C. Huang, S. Dou, Defects in metal triiodide perovskite materials towards high-performance solar cells: Origin, impact, characterization, and engineering. *Chem. Soc. Rev.* **47**, 4581–4610 (2018). [doi:10.1039/C7CS00868F](https://doi.org/10.1039/C7CS00868F) [Medline](#)
15. Y. Shao, Z. Xiao, C. Bi, Y. Yuan, J. Huang, Origin and elimination of photocurrent hysteresis by fullerene passivation in CH₃NH₃PbI₃ planar heterojunction solar cells. *Nat. Commun.* **5**, 5784 (2014). [doi:10.1038/ncomms6784](https://doi.org/10.1038/ncomms6784) [Medline](#)
16. Y. Hu, E. M. Hutter, P. Rieder, I. Grill, J. Hanisch, M. F. Aygüler, A. G. Hufnagel, M. Handloser, T. Bein, A. Hartschuh, K. Tvingstedt, V. Dyakonov, A. Baumann, T. J. Savenije, M. L. Petrus, P. Docampo, Understanding the role of cesium and rubidium additives in perovskite solar cells: Trap states, charge transport, and recombination. *Adv. Energy Mater.* **8**, 1703057 (2018). [doi:10.1002/aenm.201703057](https://doi.org/10.1002/aenm.201703057)
17. I. Levine, O. G. Vera, M. Kulbak, D.-R. Ceratti, C. Rehermann, J. A. Márquez, S. Levchenko, T. Unold, G. Hodes, I. Balberg, D. Cahen, T. Dittrich, Deep defect states in wide-band-gap ABX₃ halide perovskites. *ACS Energy Lett.* **4**, 1150–1157 (2019). [doi:10.1021/acsenergylett.9b00709](https://doi.org/10.1021/acsenergylett.9b00709)
18. C. M. Sutter-Fella, D. W. Miller, Q. P. Ngo, E. T. Roe, F. M. Toma, I. D. Sharp, M. C. Lonergan, A. Javey, Band tailing and deep defect states in CH₃NH₃Pb(I_{1-x}Br_x)₃ perovskites as revealed by sub-bandgap photocurrent. *ACS Energy Lett.* **2**, 709–715 (2017). [doi:10.1021/acsenergylett.6b00727](https://doi.org/10.1021/acsenergylett.6b00727)
19. A. Musiienko, P. Moravec, R. Grill, P. Praus, I. Vasylychenko, J. Pekarek, J. Tisdale, K. Ridzonova, E. Belas, L. Landova, B. Hu, E. Lukosi, M. Ahmadi, Deep levels, charge transport and mixed conductivity in organometallic halide perovskites. *Energy Environ. Sci.* **12**, 1413–1425 (2019). [doi:10.1039/C9EE00311H](https://doi.org/10.1039/C9EE00311H)
20. E. T. Hoke, D. J. Slotcavage, E. R. Dohner, A. R. Bowring, H. I. Karunadasa, M. D. McGehee, Reversible photo-induced trap formation in mixed-halide hybrid perovskites for photovoltaics. *Chem. Sci.* **6**, 613–617 (2015). [doi:10.1039/C4SC03141E](https://doi.org/10.1039/C4SC03141E) [Medline](#)
21. O. Hentz, Z. Zhao, S. Gradečak, Impacts of ion segregation on local optical properties in mixed halide perovskite films. *Nano Lett.* **16**, 1485–1490 (2016). [doi:10.1021/acs.nanolett.5b05181](https://doi.org/10.1021/acs.nanolett.5b05181) [Medline](#)
22. C. E. Michelson, A. V. Gelatos, J. D. Cohen, Drive-level capacitance profiling: Its application to determining gap state densities in hydrogenated amorphous silicon films. *Appl. Phys. Lett.* **47**, 412–414 (1985). [doi:10.1063/1.96129](https://doi.org/10.1063/1.96129)
23. J. T. Heath, J. D. Cohen, W. N. Shafarman, Bulk and metastable defects in CuIn_{1-x}Ga_xSe₂ thin films using drive-level capacitance profiling. *J. Appl. Phys.* **95**, 1000–1010 (2004). [doi:10.1063/1.1633982](https://doi.org/10.1063/1.1633982)
24. H.-S. Duan, W. Yang, B. Bob, C.-J. Hsu, B. Lei, Y. Yang, The role of sulfur in solution-processed Cu₂ZnSn(S,Se)₄ and its effect on defect properties. *Adv. Funct. Mater.* **23**, 1466–1471 (2013). [doi:10.1002/adfm.201201732](https://doi.org/10.1002/adfm.201201732)
25. Z. Chen, Q. Dong, Y. Liu, C. Bao, Y. Fang, Y. Lin, S. Tang, Q. Wang, X. Xiao, Y. Bai, Y. Deng, J. Huang, Thin single crystal perovskite solar cells to harvest below-bandgap light absorption. *Nat. Commun.* **8**, 1890 (2017). [doi:10.1038/s41467-017-02039-5](https://doi.org/10.1038/s41467-017-02039-5) [Medline](#)

26. D. Shi, V. Adinolfi, R. Comin, M. Yuan, E. Alarousu, A. Buin, Y. Chen, S. Hoogland, A. Rothenberger, K. Katsiev, Y. Losovyj, X. Zhang, P. A. Dowben, O. F. Mohammed, E. H. Sargent, O. M. Bakr, Low trap-state density and long carrier diffusion in organolead trihalide perovskite single crystals. *Science* **347**, 519–522 (2015). [doi:10.1126/science.aaa2725](https://doi.org/10.1126/science.aaa2725) [Medline](#)
27. Z. Chen, B. Turedi, A. Y. Alsalloum, C. Yang, X. Zheng, I. Gereige, A. AlSaggaf, O. F. Mohammed, O. M. Bakr, Single-crystal MAPbI₃ perovskite solar cells exceeding 21% power conversion efficiency. *ACS Energy Lett.* **4**, 1258–1259 (2019). [doi:10.1021/acsenergylett.9b00847](https://doi.org/10.1021/acsenergylett.9b00847)
28. S. Yang, S. Chen, E. Mosconi, Y. Fang, X. Xiao, C. Wang, Y. Zhou, Z. Yu, J. Zhao, Y. Gao, F. De Angelis, J. Huang, Stabilizing halide perovskite surfaces for solar cell operation with wide-bandgap lead oxysalts. *Science* **365**, 473–478 (2019). [doi:10.1126/science.aax3294](https://doi.org/10.1126/science.aax3294) [Medline](#)
29. H.-S. Rao, B.-X. Chen, X.-D. Wang, D.-B. Kuang, C.-Y. Su, A micron-scale laminar MAPbBr₃ single crystal for an efficient and stable perovskite solar cell. *Chem. Commun.* **53**, 5163–5166 (2017). [doi:10.1039/C7CC02447A](https://doi.org/10.1039/C7CC02447A) [Medline](#)
30. W.-Q. Wu, Z. Yang, P. N. Rudd, Y. Shao, X. Dai, H. Wei, J. Zhao, Y. Fang, Q. Wang, Y. Liu, Y. Deng, X. Xiao, Y. Feng, J. Huang, Bilateral alkylamine for suppressing charge recombination and improving stability in blade-coated perovskite solar cells. *Sci. Adv.* **5**, eaav8925 (2019). [doi:10.1126/sciadv.aav8925](https://doi.org/10.1126/sciadv.aav8925) [Medline](#)
31. B. Chen, P. N. Rudd, S. Yang, Y. Yuan, J. Huang, Imperfections and their passivation in halide perovskite solar cells. *Chem. Soc. Rev.* **48**, 3842–3867 (2019). [doi:10.1039/C8CS00853A](https://doi.org/10.1039/C8CS00853A) [Medline](#)
32. E. M. Tennyson, T. A. S. Doherty, S. D. Stranks, Heterogeneity at multiple length scales in halide perovskite semiconductors. *Nat. Rev. Mater.* **4**, 573–587 (2019). [doi:10.1038/s41578-019-0125-0](https://doi.org/10.1038/s41578-019-0125-0)
33. Q. Wang, Y. Shao, Q. Dong, Z. Xiao, Y. Yuan, J. Huang, Large fill-factor bilayer iodine perovskite solar cells fabricated by a low-temperature solution-process. *Energy Environ. Sci.* **7**, 2359–2365 (2014). [doi:10.1039/C4EE00233D](https://doi.org/10.1039/C4EE00233D)
34. Q. Jiang, Y. Zhao, X. Zhang, X. Yang, Y. Chen, Z. Chu, Q. Ye, X. Li, Z. Yin, J. You, Surface passivation of perovskite film for efficient solar cells. *Nat. Photonics* **13**, 460–466 (2019). [doi:10.1038/s41566-019-0398-2](https://doi.org/10.1038/s41566-019-0398-2)
35. T. Niu, J. Lu, M.-C. Tang, D. Barrit, D.-M. Smilgies, Z. Yang, J. Li, Y. Fan, T. Luo, I. McCulloch, A. Amassian, S. Liu, K. Zhao, High performance ambient-air-stable FAPbI₃ perovskite solar cells with molecule-passivated Ruddlesden–Popper/3D heterostructured film. *Energy Environ. Sci.* **11**, 3358–3366 (2018). [doi:10.1039/C8EE02542H](https://doi.org/10.1039/C8EE02542H)
36. Z. Yang, Z. Yu, H. Wei, X. Xiao, Z. Ni, B. Chen, Y. Deng, S. N. Habisreutinger, X. Chen, K. Wang, J. Zhao, P. N. Rudd, J. J. Berry, M. C. Beard, J. Huang, Enhancing electron diffusion length in narrow-bandgap perovskites for efficient monolithic perovskite tandem solar cells. *Nat. Commun.* **10**, 4498 (2019). [doi:10.1038/s41467-019-12513-x](https://doi.org/10.1038/s41467-019-12513-x) [Medline](#)

37. T. Matsui, T. Yamamoto, T. Nishihara, R. Morisawa, T. Yokoyama, T. Sekiguchi, T. Negami, Compositional engineering for thermally stable, highly efficient perovskite solar cells exceeding 20% power conversion efficiency with 85 °C/85% 1000 h stability. *Adv. Mater.* **31**, e1806823 (2019). [doi:10.1002/adma.201806823](https://doi.org/10.1002/adma.201806823) [Medline](#)
38. M. Burgelman, P. Nollet, S. Degrave, Modelling polycrystalline semiconductor solar cells. *Thin Solid Films* **361-362**, 527–532 (2000). [doi:10.1016/S0040-6090\(99\)00825-1](https://doi.org/10.1016/S0040-6090(99)00825-1)
39. M. Bleicher, E. Lange, Schottky-Barrier capacitance measurements for deep level impurity determination. *Solid-State Electron.* **16**, 375–380 (1973). [doi:10.1016/0038-1101\(73\)90012-9](https://doi.org/10.1016/0038-1101(73)90012-9)